# Electronic structure of Yb(III)[CH(SiMe$_3$)$_2$]$_3$ from magnetic resonance spectroscopies

Anton Ashuiev,[†] Florian Allouche,[†] José P. Carvalho,[‡] Kevin J. Sanders,[¶] Matthew P. Conley,[§] Daniel Klose,[†] Giuseppe Lapadula,[†] Michael Wörle,[†] Dirk Baabe,[‖] Marc D. Walter,[‖] Andrew J. Pell,[*,¶] Christophe Copéret,[*,†] Gunnar Jeschke,[*,†] Guido Pintacuda,[*,¶] and Richard A. Andersen[⊥]

†*Department of Chemistry and Applied Biosciences, ETH Zurich, Wolfgang-Pauli-Strasse 1-5, 8093 Zurich, Switzerland*

‡*Department of Materials and Environmental Chemistry, Stockholm University, Svänte Arrhenius väg 16 C 106 91 Stockholm, Sweden*

¶*Université Lyon, Very-High-Field NMR Center (UMR 5082 - CNRS, ENS Lyon, Université Lyon 1), F-69100 VILLEURBANNE, France*

§*Department of Chemistry and Chemical Sciences, University of California Riverside, 501 Big Springs Road, Riverside, CA 92521, USA*

‖*Institut für Anorganische und Analytische Chemie, Technische Universität Braunschweig, Hagenring 30, 38106 Braunschweig, Germany.*

⊥*Department of Chemistry, University of California, Berkeley, CA 94720, USA*

E-mail: andrew.pell@ens-lyon.fr; ccoperet@ethz.ch; gjeschke@ethz.ch; guido.pintacuda@ens-lyon.fr

**Abstract**

Characterization of paramagnetic compounds, in particular regarding the detailed conformation and electronic structure, remains a challenge - still today it often relies solely on the use of X-ray crystallography, thus limiting the access to electronic structure information. This is particularly true for lanthanide elements that are often associated with peculiar structural and electronic features in relation to their partially filled $f$-shell. Here, we showcase the use of state-of-the-art magnetic resonance spectroscopy (EPR and solid-state NMR) and computational approaches as well as magnetic susceptibility measurements to determine the structure of a paramagnetic Yb(III) alkyl complex, Yb(III)$[CH(SiMe_3)_2]_3$, that features a notable structure according to X-ray crystallography. Each of these techniques revealed specific information about the geometry and electronic structure of the complex; taken together, they provide a detailed understanding of this paramagnetic compound. Namely, this complex displays a three-centre-two-electron Yb-$\gamma$-Me-$\beta$–Si secondary metal-ligand interaction, whose NMR spectroscopic signature was acquired for the first time for a lanthanide paramagnetic species. The electronic configuration of Yb(III)$[CH(SiMe_3)_2]_3$ is demonstrated to be close to the one of the free Yb(III) ion, with the partially filled $f$-shell of the Yb atom having little influence on its bonding properties and with minimal delocalization of $f$-electron density from Yb to the directly bonded carbons.

# Introduction

Perhydrocarbyl organometallics ($MR_n$ with M = metal; R = hydrocarbyl) are a cornerstone of molecular inorganic chemistry with applications in the synthesis of catalysts and materials, and raise fundamental questions about metal–ligand bonding.[1,2] These compounds often adopt unusual geometries or bonding patterns due to their low coordination numbers and the electronic nature of the perhydrocarbyl ligands. While the Lewis structures are typically drawn with M-C $\sigma$-bonds, their reactivity patterns and spectroscopic signatures are consistent with a sizable $\pi$ character in the metal–carbon bond, indicating that alkyl groups are

better described as both $\sigma$- and $\pi$-donors to the metal.[3,4] The design strategy behind the synthesis of most homoleptic organometallics was based on choosing alkyl groups lacking $\beta$-hydrogens (to prohibit undesirable $\beta$-elimination reactions). A few examples include permethylated $M(CH_3)_4$ (M = Ti, Zr, Hf),[5–7] $Ta(CH_3)_5$,[8] $Mo(CH_3)_5$,[9] and trigonal prismatic $W(CH_3)_6$.[10–12] Neopentyl derivatives supply additional steric protection and are generally more stable than permethylated organometallics. $M(CH_2{}^tBu)_4$ (M = group 4, Cr)[13,14] contain M–C $\sigma$-bonds, while $Ta(=CH^tBu)(CH_2^tBu)_3$,[15] $M(\equiv C^tBu)(CH_2^tBu)_3$ (M = Mo, W),[16] and $Re(\equiv C^tBu)(=CH^tBu)(CH_2{}^tBu)$[17] also contain metal-carbon multiple bonds. Some of these latter complexes display quite unusual geometries due to interactions of the $\alpha$-CH with the electron deficient $d^0$ metal center.[18]

Similar design constraints are common for homoleptic organolanthanides. The lanthanides are usually in the (+3) oxidation state and prefer high coordination numbers. Larger alkyl ligands, such as the sterically bulky bis-trimethylsilylmethyl ligand, resulted in the isolation of monomeric $Ln[CH(SiMe_3)_2]_3$ (Ln = Y,[19] La,[20] Ce,[19] Sm,[20] Lu[21]) (Fig. 1a). Crystallographically characterized $Ln[CH(SiMe_3)_2]_3$ compounds contain three short $Ln\cdots C_\gamma$ contacts between one Si-$CH_3$ group of each of the three proximal $-SiMe_3$ groups. The $Ln\cdots C_\gamma$ contacts result in lengthening of the Si-$CH_3$ bonds close to the lanthanide by $\sim 0.04$ Å with respect to the other Si-$CH_3$, indicating that these proximal Si-$CH_3$ groups interact with the lanthanide. This interaction helps to satisfy the high coordination numbers required to isolate these $f$-block homoleptic complexes; a strategy that also facilitates isolation of $Yb[C(SiMe_3)_3]_2$,[22] $Ln(AlMe_4)_3$,[23] and $Ln[C(SiHMe_2)_3]_2$.[24,25]

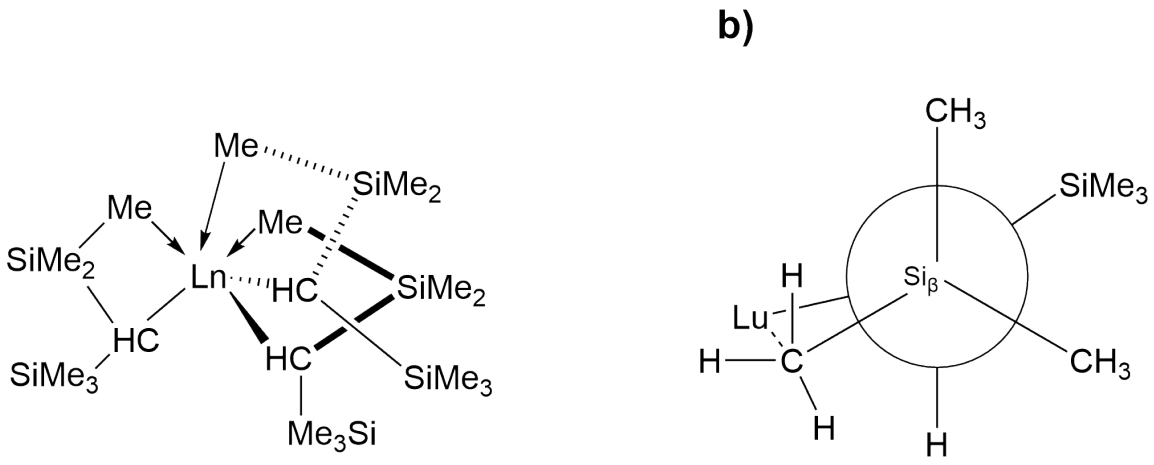


Figure 1: (a) Typical structure of monomeric $Ln[CH(SiMe_3)_2]_3$ species, together with secondary $Ln^{\cdots}C_\gamma$ interactions indicated by arrows. (b) Newman projection viewed down the $Si_\beta$ - $C_\alpha$ bond, showing the $Lu^{\cdots}C_\gamma$-$Si_\beta$ interaction in the $Lu[CH(SiMe_3)_2]_3$ compound.[21]

Detailed studies of $Lu[CH(SiMe_3)_2]_3$[21] described the nature of the interaction between lutetium and the proximal Si–$Me_3$ groups. High quality X-ray diffraction data showed that C–H bond lengths and angles at the proximal Si–$CH_3$ engaged in the $Ln\cdots C_\gamma$ contacts were values expected for tetrahedral carbon. Variable temperature solution nuclear magnetic resonance (NMR) data showed that Lu–C rotation in $Lu[CH(SiMe_3)_2]_3$ was slow on the NMR timescale at –140°C in 2-methylbutane-d[12] and $^1J_{CH}$ of the proximal and distal –$SiMe_3$ groups were both 117 ± 1 Hz. In the solid state, $^{13}C$ cross-polarisation magic-angle spinning (CPMAS) NMR spectra contain three –$SiMe_3$ peaks, consistent with slow Lu–C and slow Si–C rotation in the crystalline solid. Solid-state $J$-resolved $^1H$–$^{13}C$ NMR spectra showed that all $^1J_{CH}$ coupling constants were essentially identical (117 ± 4 Hz). Density functional theory (DFT) models of $Lu[CH(SiMe_3)_2]_3$ reliably reproduce the structural and spectroscopic trends obtained experimentally and natural bond orbital (NBO) analysis shows that the charges on $C_\alpha$ and $C_\gamma$ are negative, while the charges on $Si_\beta$ and $H_\gamma$ are positive. These results indicate that the $Lu\cdots C_\gamma$ interactions are not a result of C–H agostic interactions (2-electron donation from a C-H bond to an electron deficient metal center),[26] but are rather due to a three-center-two-electron (3c-2e) interaction between the Si–Me and Lu. In other words, the $Lu\cdots C_\gamma$ interaction is best described as a pseudo bridging Lu–Me–Si group (Fig.

1b), analogous to Al–Me–Al observed in dimeric $AlMe_3$[27,28] or $Ln(AlMe_4)_3$.[29]

In contrast to Lu (and La), the intermediate Ln series are paramagnetic and have a partially filled $f$-shell. This raises questions of whether $Ln\cdots C_\gamma$ interactions in paramagnetic lanthanides can be described similarly to those discussed for Lu, and if additional partial electron transfer processes are possible considering that some lanthanides adopt multiconfigurational ground states. For instance, multiconfigurational states are present in compounds as simple as $Ce(acac)_3$ that are actually ground-state mixtures of $f^1$-$Ce^{3+}$ and $f^0$-$Ce^{4+}$.[30] This also appears to be fairly common in the chemistry of organoytterbium compounds. $Cp^*_2Yb(bipy)$ is an admixture of $f^{14}$-Yb(II)(bipy) and $f^{13}$-Yb(III)$(bipy)^{\cdot-}$,[31–33] $Cp_3Yb$ contains ∼14% of the charge transfer $f^{14}$-Yb(II)$(Cp_3)^{1-}$,[34] and $[Cp^*_2Yb]_2(\mu{-}Me)$ and $[Cp^*_2Yb]_2(\mu{-}H)$ are multi-configurational doublets containing a delocalized electron in a $d_{z^2}$ orbital on Yb.[35] Such specific configurations have been proposed to explain the lack of reactivity of $[Cp^*_2Yb]_2(\mu{-}Me)$ towards olefins, compared to the Lu equivalent $Cp^*_2$Lu-Me.[36,37]

$Yb[CH(SiMe_3)_2]_3$ was previously mentioned as a synthetic intermediate, but was not characterized.[38] This study describes the syntheses of $Yb[CH(SiMe_3)_2]_3$, $Yb[CH(SiMe_3)_2]_2[O{-}2,6{-}t Bu_2{-}C_6H_3]$ and $Yb[CH(SiMe_3)_2][O{-}2,6{-}t Bu_2{-}C_6H_3]_2$. X-ray diffraction analysis shows that all compounds contain short $Yb\cdots C_\gamma$ contacts, and further stimulates to understand the nature of that interaction in these paramagnetic complexes.

Magnetic Resonance spectroscopies such as NMR and Electron Paramagnetic Resonance (EPR) are in principle uniquely positioned to access molecular and electronic structures at atomic resolution. However, Yb(III) is difficult to study using NMR, as the unpaired electrons have strong hyperfine couplings to the surrounding nuclei, which have the effect of inducing very broad signals with short relaxation times often impossible to detect. In addition, the short electronic spin relaxation times and large hyperfine couplings make also the EPR signals not detectable at room temperatures using routine continuous wave (CW) methods.

Over the last twenty years, spectacular progress has been made in the development of

instrumentation and spectroscopic methods in both NMR and EPR, which allows us to start targeting these paramagnetic lanthanide complexes. Specifically, solid-state NMR with fast magic-angle spinning (MAS) and broadband adiabatic irradiation sequences[39] can now be used to obtain data of microcrystalline powders. Similarly, EPR has seen impressive progress in the development of pulsed techniques.[40] In parallel, the recent advances in quantum chemical/density functional theory (DFT) methods and dedicated formalisms[41–46] allow today to interpret NMR and EPR data in terms of the spatial and electronic structure of paramagnetic complexes.[47–53]

In this study we explore the use of the most advanced available EPR, solid-state NMR and quantum chemical calculation approaches for the full molecular and electronic structure characterization of $Yb[CH(SiMe_3)_2]_3$, as a prototypical organolanthanide compound to understand the nature of the $Yb\cdots C_\gamma$ contacts. All these methods point out that the short $Yb\cdots C_\gamma$ contact in $Yb[CH(SiMe_3)_2]_3$ is best discussed as a 3c-2e Yb-Me-Si interaction without involvement of the Yb $f$-electrons in this bonding.

# Results and discussion

## Synthesis and X-ray diffraction studies of $Yb[CH(SiMe_3)_2]_3$

The syntheses of $Yb[CH(SiMe_3)_2]_3$, together with $Yb[CH(SiMe_3)_2]_2[O{-}2,6{-}tBu_2{-}C_6H_3]$ and $Yb[CH(SiMe_3)_2][O{-}2,6{-}tBu_2{-}C_6H_3]_2$, are shown in Fig. 2a (see SI Section 1 for detailed synthetic procedures). Similar to the lutetium complexes isolated previously,[21] the alkylation depends on the stoichiometry of the organolithium reagent. A key to successful isolation of these compounds is sufficient volumes of pentane to dissolve the sparingly soluble polymeric $Li[CH(SiMe_3)_2]$.[54] Addition of $Li[CH(SiMe_3)_2]$ as a slurry in smaller volumes of pentane results in poor yields and formation of mixtures of these compounds. All organoytterbium compounds shown in Fig. 2a are isolated as crystalline solids from concentrated pentane solutions. $Yb[CH(SiMe_3)_2]_3$ is blue, $Yb[CH(SiMe_3)_2]_2[O{-}2,6{-}tBu_2{-}C_6H_3]$ is brown, and

$Yb[CH(SiMe_3)_2][O{-}2,6{-}tBu_2{-}C_6H_3]_2$ is red. The study below focuses on the structure and spectroscopic features of $Yb[CH(SiMe_3)_2]_3$. X-ray structures of $Yb[CH(SiMe_3)_2]_2[O{-}2,6{-}tBu_2{-}C_6H_3]$ and $Yb[CH(SiMe_3)_2][O{-}2,6{-}tBu_2{-}C_6H_3]_2$ are provided in SI Chapter 2.2 (see Figs. S3 - S6), and their NMR spectra are provided in SI Chapter 7 (see Figs. S14 - S19).

A view of the $Yb[CH(SiMe_3)_2]_3$ complex is shown in Figs. 2a & S2. The relevant bond distances obtained from this structure are shown in Fig. 2c-d (see also Tab. S2). For comparison the previously reported bond distances for $Lu[CH(SiMe_3)_2]_3$[21] (Fig. 2e) are also shown in Fig. 2f-g (see also Tab. S2). $Yb[CH(SiMe_3)_2]_3$ crystallizes in the $P31_c$ space group and is isostructural with other isolated $Ln[CH(SiMe_3)_2]_3$. $Yb[CH(SiMe_3)_2]_3$ adopts a C3 symmetric structure with the ytterbium displaced from the plane defined by the three Yb-C bonds by 0.783(3) Å. The Yb–$C_\alpha$ (Yb-$C_1$) distance is 2.324(3) Å, which is nearly the same as the Lu-$C_\alpha$ distance in $Lu[CH(SiMe_3)_2]_3$ (2.319(3) Å) and the Sm-$C_\alpha$ distance in $Sm[CH(SiMe_3)_2]_3$ (2.33(2) Å).

$Yb[CH(SiMe_3)_2]_3$ contains short Yb$\cdots$$C_\gamma$ contacts at 2.963(3) Å, which is slightly longer than Lu$\cdots$$C_\gamma$ (2.936(2) Å) and Sm$\cdots$$C_\gamma$ (2.85(3) Å) distances in $Lu[CH(SiMe_3)_2]_3$ and $Sm[CH(SiMe_3)_2]_3$, respectively. The Neumann projection shown in Fig. 2d contains distances and angles for the proximal Si–$CH_3$ group interacting with Yb. The C–H bond distances and angles are close to those expected for a tetrahedral $sp^3$ hybridized carbon, again similar to results obtained for $Lu[CH(SiMe_3)_2]_3$. These structural data infer that a similar 3c-2e Yb–Me–Si interaction is present in $Yb[CH(SiMe_3)_2]_3$ under the conditions of low-temperature X-ray diffraction studies (i.e. 100 K).

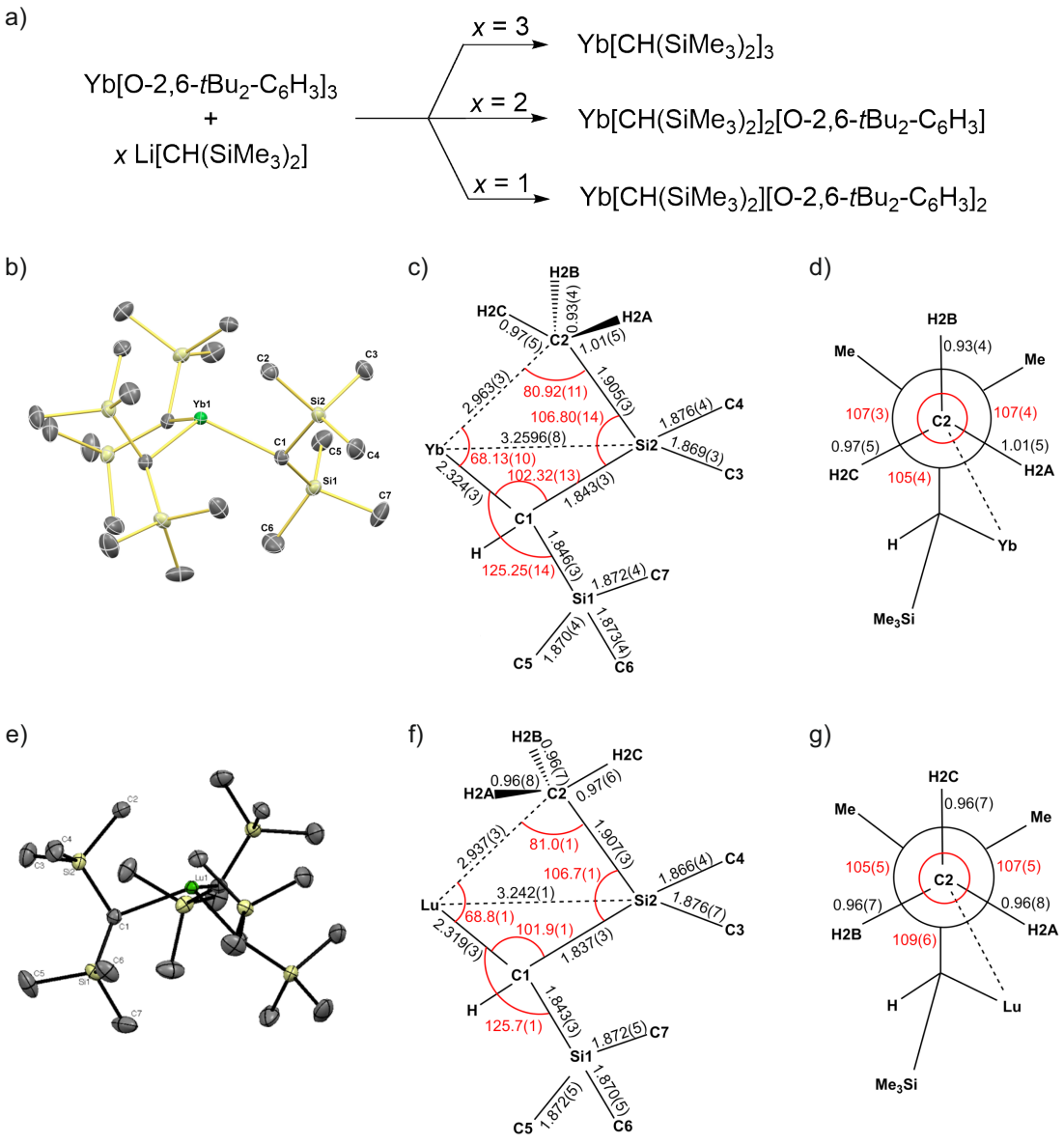


Figure 2: (a) Synthesis scheme of $Yb[CH(SiMe_3)_2]_x[O\text{-}2,6\text{-}t\mathrm{Bu}_2\text{-}C_6H_3]_{3-x}$ ($x$ = 1, 2, 3). (b) Structure of the $Yb[CH(SiMe_3)_2]_3$ complex with displacement ellipsoids at 50 % probability level. For clarity the hydrogen atoms and the solvent molecules $CH_2(SiMe_3)_2$ are omitted. (c) Sketch of relevant bond lengths and angles of $Yb[CH(SiMe_3)_2]_3$. The bond lengths are reported in Å, and the bond angles (in red) are reported in degrees (see also Tab. S2). (d) Newman projection down the C(2)–Si(2) bond with bond lengths and angles (in red) obtained from the crystal structure of $Yb[CH(SiMe_3)_2]_3$. (e) Structure of the $Lu[CH(SiMe_3)_2]_3$ complex with displacement ellipsoids at 50 % probability level. For clarity the hydrogen atoms and the solvent molecules $CH_2(SiMe_3)_2$ are omitted. (f) Sketch of relevant bond lengths and angles of $Lu[CH(SiMe_3)_2]_3$. The bond lengths are reported in Å, and the bond angles (in red) are reported in degrees (see also Tab. S2) (f) Newman projection down the C(2)–Si(2) bond with bond lengths and angles (in red) obtained from the crystal structure of $Lu[CH(SiMe_3)_2]_3$. For comparison panels e)-g) are reproduced with permission from Conley et al.[21] .

## Magnetic susceptibility studies on $Yb[CH(SiMe_3)_2]_3$

We performed magnetic susceptibility studies for all ytterbium compounds $Yb[CH(SiMe_3)_2]_3$, $Yb[CH(SiMe_3)_2]_2[O{-}2,6{-}t Bu_2{-}C_6H_3]$, $Yb[CH(SiMe_3)_2][O{-}2,6{-}t Bu_2{-}C_6H_3]_2$, and $Yb[O{-}2,6{-}t Bu_2{-}C_6H_3]_3$ (see SI Chapter 6, Figs. S10 - S13 and Tab. S15 for more details). All four ytterbium complexes exhibit experimental values of the effective magnetic moment at 300 K that are in the range between $\mu_{eff}$(300 K) = 4.30 $\mu_B$ ($\chi$T = 2.31 cm$^3$ K mol$^{-1}$) and 4.53 $\mu_B$ ($\chi$T = 2.57 cm$^3$ K mol$^{-1}$). In particular, the effective magnetic moment of the $Yb[CH(SiMe_3)_2]_3$ complex is $\mu_{eff}$(300 K) = 4.53 $\mu_B$. These values are in good agreement with the expectation value of free Yb(III) ion, described by a single $^2F_{7/2}$ term ($4f^{13}$), for which $\mu_{eff}$(300 K) = 4.54 $\mu_B$ ($\chi$T = 2.58 cm$^3$ K mol$^{-1}$). Hence all Yb complexes including $Yb[CH(SiMe_3)_2]_3$ can be described by a single $4f^{13}$ configuration, similar to those of the free Yb(III) ion.

## EPR characterization of the $Yb[CH(SiMe_3)_2]_3$ complex

We characterized the Yb(III) alkyl complex $Yb[CH(SiMe_3)_2]_3$ by EPR spectroscopy, which has seen an impressive progress in the development of pulsed techniques[40] and which, together with computational studies, has enabled the successful characterization of the spatial and electronic structure of paramagnetic complexes.[34,53] The continuous-wave (CW) EPR spectrum of $Yb[CH(SiMe_3)_2]_3$ (Fig. 3a, blue) was reasonably reproduced by simulation (Fig. 3a, red) by modeling the Yb ion as an electronic spin $S = 1/2$, with $g$ tensor principal values of $g_\perp = 0.7316$ and $g_\parallel = 7.5698$. The spectrum also exhibits a well-resolved satellite structure, due to hyperfine coupling to the two spin-active isotopes $^{171}$Yb (spin $I = 1/2$ and natural abundance of 14.31%) and $^{173}$Yb (spin $I = 5/2$ and natural abundance of 16.13%) of the lanthanide. From spectral simulation (Fig. 3a, red), the $^{171,173}$Yb hyperfine tensors were determined to be $A_\perp(^{173}\text{Yb})$ = 221 MHz, $A_\parallel(^{173}\text{Yb})$ = 1650 MHz, and accordingly $A_\perp(^{171}\text{Yb})$ = 842 MHz, $A_\parallel(^{171}\text{Yb})$ = 6285 MHz.

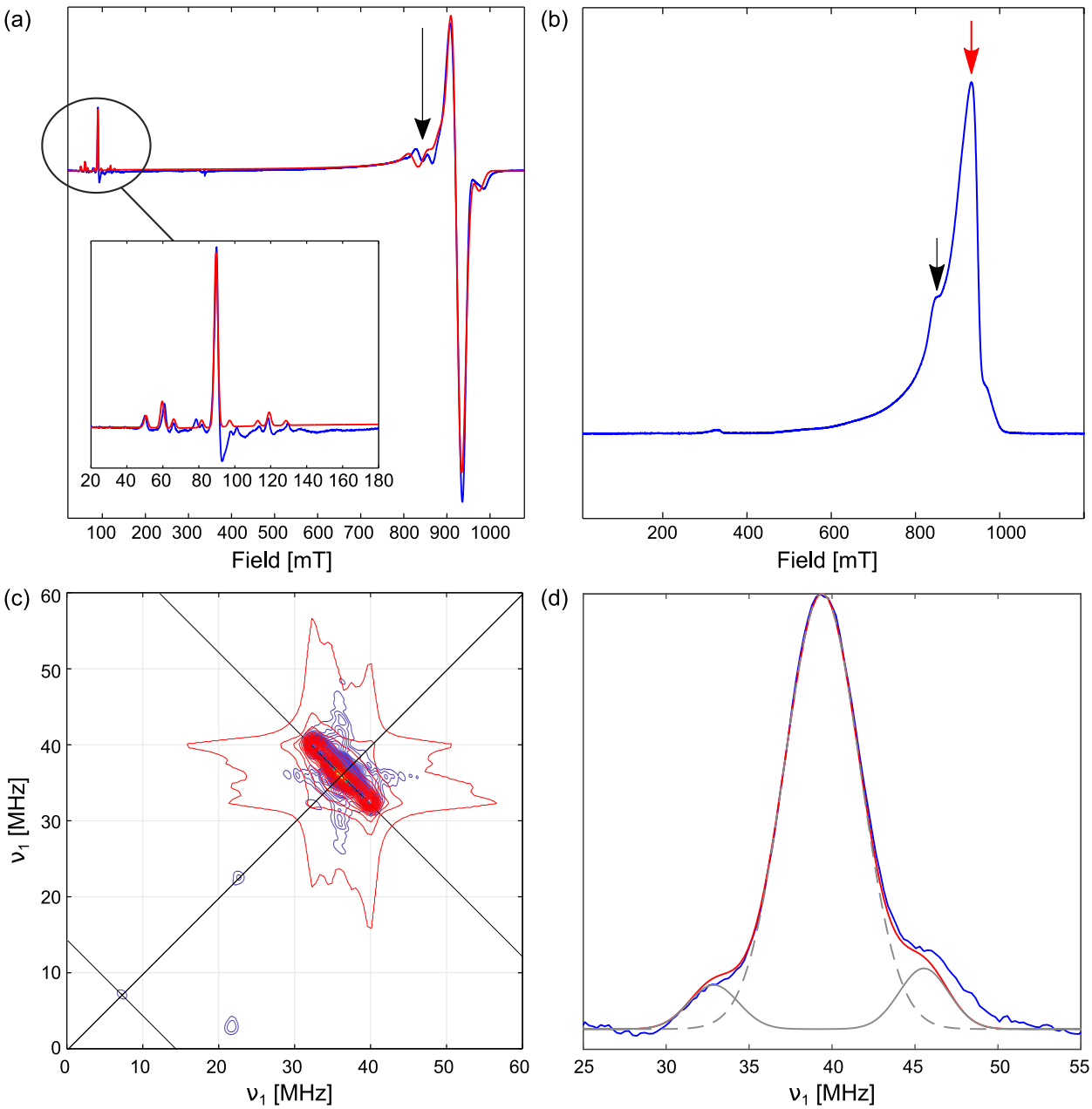


Figure 3: (a) CW EPR spectrum of $Yb[CH(SiMe_3)_2]_3$ (blue) and simulation (red), together with an expansion of the low-field region. The black arrow marks the field position of the HYSCORE measurement. (b) Echo-detected EPR spectrum of $Yb[CH(SiMe_3)_2]_3$. The field position for HYSCORE and EDNMR are marked with a black and red arrow, respectively. (c) HYSCORE spectrum of $Yb[CH(SiMe_3)_2]_3$ (blue to yellow, see also Fig. S8) and simulation (red) based on a single $^1$H hyperfine coupling $A_{iso}(^1H) = 3.8 \pm 0.3$ MHz. Anti-diagonal lines indicate the $^1$H and $^{29}$Si nuclear Zeeman frequencies. Spurious peaks at 21.5/2.0 MHz and 23.5/23.5 MHz are electronic artefacts. (d) $^1$H region of EDNMR spectrum of $Yb[CH(SiMe_3)_2]_3$ (blue), together with simulation (red) of a single effective $^1$H coupling with $A_{eff}(^1H) = 13 \pm 1$ MHz (gray) and a $^1$H matrix peak (gray dashed) at a $^1$H nuclear Zeeman frequency of 39.4 MHz.

A higher-resolution picture can be provided by pulsed EPR spectroscopy, which has evolved into a robust tool for the determination of geometry and electronic configuration of organometallic complexes of paramagnetic *d*- and *f*-block metals. In particular, 2D hyperfine sub-level correlation spectroscopy (HYSCORE)[55] allows us to detect magnetically active nuclei (e.g. $^{1}$H, $^{13}$C, $^{29}$Si etc.) that are coupled to paramagnetic centers by hyperfine interaction, due to close spatial proximity to these centers. The technique can separate the isotropic (primarily Fermi-contact) and anisotropic (primarily spin-dipolar) parts of the hyperfine interaction tensors that are linked to the electronic properties of the systems (e.g. metal-ligand spin density transfer), and bonding between the nuclei and the paramagnetic center. The HYSCORE spectrum of Yb[CH(SiMe$_3$)$_2$]$_3$ (Fig. 3c and Fig. S8) reveals the presence of hyperfine coupling to protons in the CH(SiMe$_3$)$_2$ alkyl ligands. From the simulation of the HYSCORE spectrum a single $^{1}$H hyperfine tensor was determined to have $A_{\mathrm{iso}}(^{1}\mathrm{H}) = 3.8 \pm 0.3$ MHz, $T_{\mathrm{dip}}(^{1}\mathrm{H}) = 4.0 \pm 0.5$ MHz ($A_{\mathrm{dip}} = [-4.0 \pm 0.5; -4.0 \pm 0.5; 8.0 \pm 1.0]$ MHz), with the tensors principal axis system rotated by $45^{\circ} \pm 15^{\circ}$ with respect to the $z$ axis of the principal axis system of the $g$ tensor. This interpretation of the HYSCORE data is consistent with the ELDOR-detected NMR (EDNMR)[56] spectrum shown in Fig. 3d, from which we can extract a single splitting due to an effective hyperfine coupling to $^{1}$H with $A_{\mathrm{eff}}(^{1}\mathrm{H}) = 13 \pm 1$ MHz. Based on previous observations of similar isotropic and dipolar parts of hyperfine coupling tensors for the $S = 1/2$ Ti(III) alkyl complexes,[53,57] the observed $^{1}$H hyperfine couplings could be assigned to the hydrogen atoms that are close in space to the Yb(III) center, such as $\alpha$-H atoms of CH(SiMe$_3$)$_2$ ligands. This finding indicates that the transferred spin density is significant only for the closest to the Yb(III) atoms, such as $C_1$ and $H_1$, while it is substantially lower for the rest of the ligands. The observed isotropic $^{1}$H hyperfine couplings that are even smaller than those observed for d$^1$ metal alkyls[53,57] suggest that, in contrast to the case of Cp$_3$Yb,[34] there is no significant charge and spin density transfer to the ligands in Yb[CH(SiMe$_3$)$_2$]$_3$. This is also consistent with the preferential presence of the unpaired electron in the $4f$ orbital rather than in the valence $5d$ orbital,

which would result in more significant distribution of the spin density into the ligands of Yb(III). A difficulty of promoting $4f$ electrons of Yb(III) to the $5d$ orbital, which effectively prevents the formation of double Yb=C bonds, was previously discussed based on CASSCF calculations.[37] Taking into account the results of magnetic susceptibility measurements, we propose that the ground state of the $Yb[CH(SiMe_3)_2]_3$ complex has a single electronic configuration of $4f^{13}$ (S = 1/2), close to the one of Yb(III) free ion, consistent with the magnetic susceptibility measurements (vide supra).

## DFT-optimized geometry

Since the electronic structure of Yb in $Yb[CH(SiMe_3)_2]_3$ is described by a single $4f^{13}$ (S = 1/2) configuration, we carried out a geometry optimization of $Yb[CH(SiMe_3)_2]_3$ structure at the DFT level of theory as a first step to clarify whether it exhibits the same geometry and bonding motif between the Yb center and the $C_2$ atom as in the previously characterized $Lu[CH(SiMe_3)_2]_3$.[21] The structure was computed for a single molecular complex. It was optimized using the low-temperature X-ray coordinates as a starting point, and using the PBE0[58–60] functional with D3BJ dispersion correction[61] and considering the relativistic ZORA Hamiltonian[62] (see SI Chapter 1.8 for more details). Symmetry restrictions were not enforced during the geometry optimization, unveiling an optimized molecular geometry which deviates slightly from ideal $C_{3v}$ point-group symmetry. Specifically, the three ligands have different spatial relationship relative to the Yb, as shown in Fig. S9. This effect, as well as the shortened Yb-C-H angles for the $\alpha$-H atoms of the $[CH(SiMe_3)_2]_3$ ligands (Fig. S9 & Tab. S7), might be explained by a simultaneous electrostatic repulsion from the Yb center and the two Si atoms of the $CH(SiMe_3)_2$ ligand. A similar effect was previously observed for the $[CH(SiMe_3)_2]_3$ ligands of the Lu(III)[21] or Ti(III) analogues.[57] This is consistent with a progressive helical rotation of the three ligands at low temperature (the DFT structure corresponds to a nominal $T$ of 0 K). This deviation from $C_{3v}$ symmetry is not evident from the X-ray structure; nevertheless, the close proximity of $Si_2$ to Yb compared to $Si_1$ is reproduced

in the calculated structure. In order to interpret these results, we calculated the EPR parameters ($g$ tensor and magnetic susceptibility) for the relativistic DFT optimized structure (see Fig. S9), using multi-reference perturbation theory (CASSCF/NEVPT2)[63–68] and considering a single $S = 1/2$ $4f^{13}$ configuration and an active space comprising only of $f$ orbitals, CAS(13,7), including both scalar relativistic effects, using the second order Douglas-Kroll-Hess Hamiltonian,[69] as well as spin-orbit coupling (see SI Chapter 1.8 for more details). The results are summarized in Tab. 1. The calculated $g$ tensor agrees well with the experiments, which constitutes additional evidence that the complex can be well described with a single configuration and that our proposed relativistic DFT optimized geometry is consistent with the EPR characterization. Calculations additionally yield the isotropic magnetic susceptibility, which compares favorably with that determined experimentally (see Tab. 1 & Fig. S10). This allows us to confirm that the ground state of the $Yb[CH(SiMe_3)_2]_3$ complex has a single electronic configuration of $4f^{13}$ ($S = 1/2$), close the one of the free ion.

Table 1: Comparison of experimental and calculated $g$ tensor ($g_x$, $g_y$ and $g_z$ represent the components of $g$ tensor its principal axes frame) and magnetic properties of the $Yb[CH(SiMe_3)_2]_3$ complex. Calculated values were obtained using multi-reference perturbation theory (CASSCF/NEVPT2). Experimental values were obtained via EPR characterization and magnetic measurements.

| | Experiment | Calculated |
|---|---|---|
| $g_x$ | 0.7316 | 0.6544 |
| $g_y$ | 0.7316 | 0.6559 |
| $g_z$ | 7.5698 | 7.7972 |
| $\chi T$ (300 K) [$cm^3$ K $mol^{-1}$] | 2.57 | 2.34 |

We also calculated the hyperfine coupling tensors for all the spin-active nuclei in the ligands (Tab. S9). These tensors were calculated using spin-component scaled MP2[70,71] and DFT using the PBE0 functional.[58–60] Predicting the hyperfine coupling in lanthanide systems is extremely challenging since it requires that the method is able to reproduce the spin-density correctly. DFT based approaches are inherently limited by the self-interaction error which may compromise their accuracy.[72–74] For this reason we also employed a post Hartree-Fock wave function based method in order to ensure the consistency of our calculations. From

these results we can tentatively assign the hyperfine interactions observed by HYSCORE and EDNMR to $H_1$ atoms, which has computed isotropic values in the range of $-1.44$ to 0.51 MHz, while all the rest exhibit a magnitude below 0.13 MHz. The quantitative discrepancy with experiments is due to the proximity of $H_1$ to Yb, which requires high-level relativistic electronic structure methods for accurate determination of the spin polarization and spin delocalization and the multireference character of the wave function.[75] Nevertheless, our tentative assignment is supported by the calculated approximately axial spin-dipolar hyperfine coupling tensor of $T_{\mathrm{dip}}(^1\mathrm{H}_1)$ $\sim$4 MHz, which is in very good agreement with the experiments. This indicates that the positions of the $\alpha$-H ($H_1$) atoms of the $CH(SiMe_3)_2$ ligands of $Yb[CH(SiMe_3)_2]_3$, including the related Yb-H distances and the Yb-C-H angles (see Tab. S7), are nicely reproduced within the relativistic DFT optimized structure, shown in Fig. S9.

## NMR characterization of $Yb[CH(SiMe_3)_2]_3$ complex

Over the last twenty years, the development of instrumentation and spectroscopic methods in NMR allows us to target paramagnetic lanthanide complexes such as $Yb[CH(SiMe_3)_2]_3$. Specifically, solid-state NMR with fast magic-angle spinning (MAS) and broadband adiabatic irradiation sequences[39] can now be used to obtain data of microcrystalline powders, where the complex dynamics are simplified and only the relevant internal ligand motions are retained. Nonetheless, obtaining high-quality magnetic resonance data on these systems represents only part of the challenge, since the resulting spectra are often very difficult to interpret using standard textbook assignment methods. In this respect, recent progress in quantum chemical/density functional theory (DFT) methods for the computation of NMR parameters of paramagnetic complexes has also been impressive. For NMR, there have been significant advances both in the development of the formalism of the paramagnetic shifts[41–46] and the computational implementation.[47–52] However, the application of the developed methods on lanthanides has been representing a much more daunting prospect so far.

For the $Yb[CH(SiMe_3)_2]_3$ complex, we have drawn the conclusions regarding its electronic structure and on the positions of $^1H$ nuclei closest to the metal center ($H_1$) based on the EPR data and relativistic quantum chemistry calculations. However, the weak hyperfine interactions between the unpaired electron and the more distant nuclei prevented us from obtaining any high-resolution information about the rest of the molecule by EPR spesctroscopy. This gap could, however, be filled by paramagnetic NMR spectroscopy.[39]

The ligands of the complex are expected to exhibit substantial dynamics, which has the effect of averaging the signals. This was observed in the case of the Lu analogue, where variable temperature $^1H$ solution NMR was required to freeze out these motions and the individual $^1H$ resonances were obtained by cooling the sample. However, this approach was not successful for the present Yb complex, where no such resolution was obtained over a temperature range between 285 and 182 K, and no detection was possible beyond that because of increased line-broadening due to enhanced relaxation (see SI Chapter 3 & Fig. S7).

We therefore proceeded to examine the $Yb[CH(SiMe_3)_2]_3$ complex via solid-state magic-angle spinning (MAS) NMR, which has the advantage of eliminating molecular rotation diffusion, so that only the internal ligand dynamics are present. Such spectra relate to the room-temperature crystal structure, thereby providing a direct bridge to the low-temperature XRD data.

One-dimensional solid-state MAS NMR spectra of $^1H$, $^{13}C$ and $^{29}Si$ are shown in Fig. 4a-c. Each of these spectra exhibits poorly resolved patterns, due to hyperfine interactions with the unpaired electron, which induce large shifts and shift anisotropies and extremely large inhomogeneous line-broadenings. We see shift anisotropies that are very large for all three nuclei, of the order of hundreds of ppm, in contrast to the Lu analogue, where the $^1H$ and $^{13}C$ diamagnetic chemical shift anisotropies (CSAs) were too small to be measured and for $^{29}Si$ were of the order of tens of ppm. In particular, for the Lu analogue, $^{29}Si$ CSAs were used to characterize the metal-ligand interaction. That approach is not applicable to the

paramagnetic Yb complex, since the interpretation of the shift anisotropy is more complex.

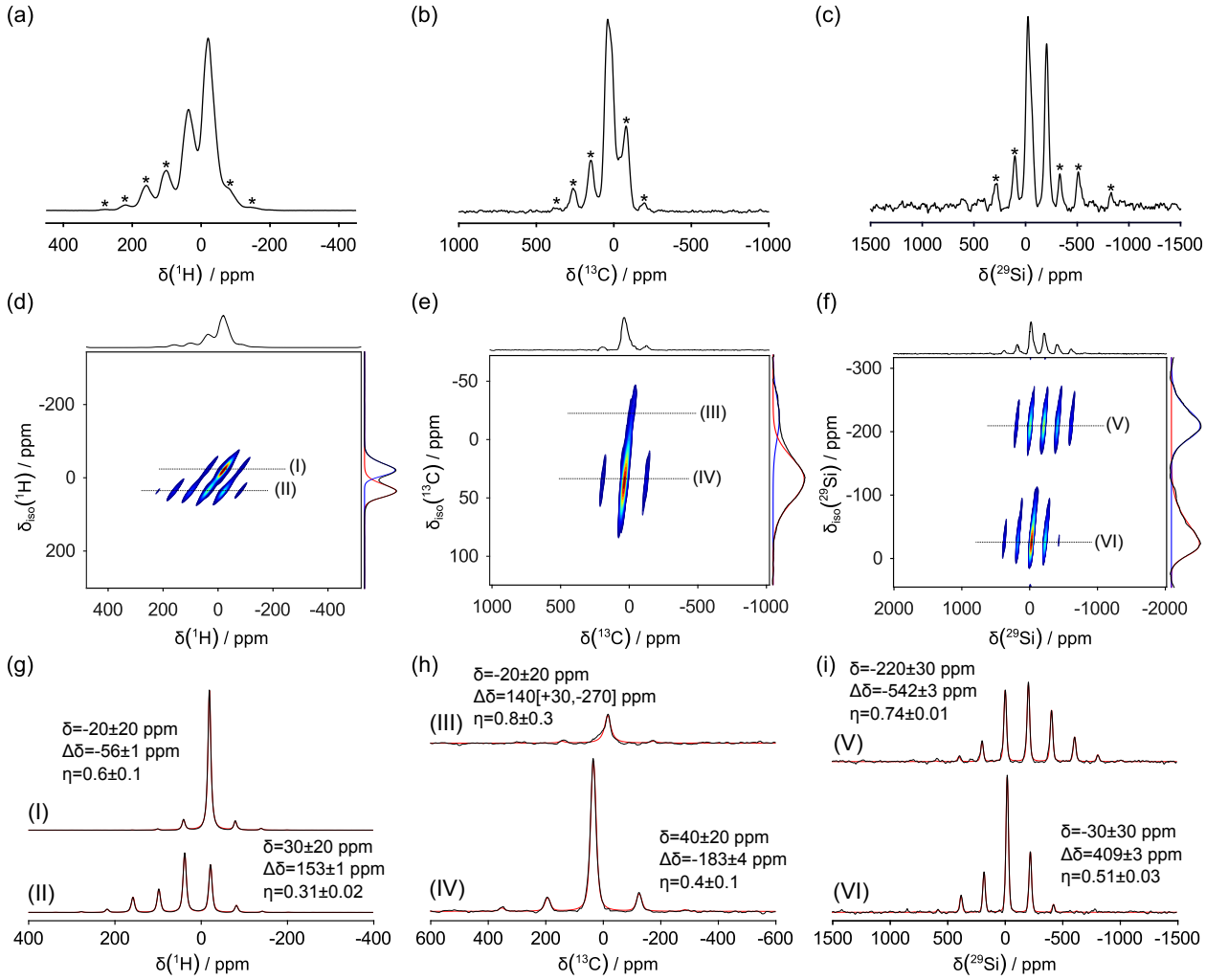


Figure 4: NMR spectra of $Yb[CH(SiMe_3)_2]_3$: (a) $^1$H MAS spectra at 30 kHz MAS,(b) $^{13}$C MAS spectra of at 14.286 kHz MAS and (c) $^{29}$Si MAS spectra at 30 kHz MAS, showing two distinct $^{29}$Si signals. The spinning sidebands are marked with asterisks ($*$). 2D aMAT spectrum: (d) $^1$H at 30 kHz, (e) $^{13}$C at 20 kHz and (f)$^{29}$Si at 20 kHz. The indirect dimension projections were deconvolved using asymmetric Gaussian functions to extract the isotropic shifts and quantify shift dispersion. (g)-(i) extracted slices with isotropic shift corresponding to the maxima of the deconvolved projections and labelled with Roman numerals. Each slice was subsequently fitted considering a simple CSA model using the Haeberlen convention[76] ($\delta_{\mathrm{iso}} = \frac{1}{3}(\tilde{\delta}_{xx} + \tilde{\delta}_{yy} + \tilde{\delta}_{zz})$, $\Delta\delta = \tilde{\delta}_{zz} - \delta_{\mathrm{iso}}$ and $\eta = (\tilde{\delta}_{yy} - \tilde{\delta}_{xx})/\Delta\delta$, where $\delta_{xx}$, $\delta_{xx}$ and are the components of the CSA tensor in the principal axes frame). See SI chapter 1.6 for more details.

The first problem to be addressed is the lack of resolution of the individual signals in each of the three spectra, due to the overlapping spinning sideband manifolds of neighboring res-

onances. To solve this problem, we employed the 2D adiabatic magic-angle turning (aMAT) experiment,[77] which correlates each spinning side-band manifold to its isotropic shift, thus removing the overlap, as seen in Fig. 4d-f for $^{1}$H, $^{13}$C and $^{29}$Si, respectively. In all three cases, the aMAT spectra are able to resolve two resonances with distinct isotropic shifts. For $^{29}$Si, the interpretation is relatively straightforward, with the two signals V and VI being due to the two inequivalent Si nuclei (specifically, one due to $Si_1$ and the other to $Si_2$). By extension, it is reasonable to tentatively interpret each $^{13}$C signal (III and IV) as being from the three methyl groups attached to each of the Si ($C_{2/3/4}$ and $C_{5/6/7}$), and each $^{1}$H signal (I and II) to the corresponding group of protons ($H_{2/3/4}$ and $H_{5/6/7}$).

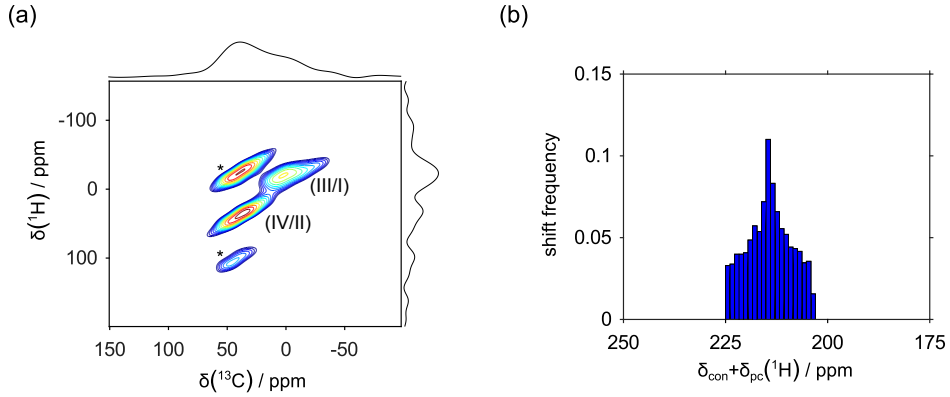


Figure 5: (a) $^{1}$H-$^{13}$C correlation spectrum achieved by using the TEDOR experiment[78] at 30 kHz MAS, yielding two distinct correlations of the resonances (III/I) and (IV/II), shown in Fig. 4, which were subsequently used to model the paramagnetic shifts in the following section. The spinning sidebands are marked with asterisks (∗). (b) $^{1}$H NMR shift distributions considering solely the contributions arising from the presence of the unpaired electron and neglecting long-range PCS effects stemming from parametric centers in neighboring unit cells ($\delta_{\mathrm{con}} + \delta_{\mathrm{pcs}}$). The shifts were calculated considering the Moon and Patchkovski[41] and Vaara et a.[42–44] formalism using the $g$ tensor obtained using multi-reference perturbation theory and the experimental $^{1}$H hyperfine tensor. A distribution of relative orientations of the $g$ and $A$ tensors were considered using Zaremba, Conroy, Wolfsberg orientational averaging scheme with 1154 orientations.[79–81] The relative orientation of the $z$ axes of the $g$ and $A$ tensors was kept fixed at 45°, in order to match with the EPR results.

For each of the signals I-VI, a slice extracted from the aMAT spectra was fitted to determine the parameters of the shift tensor (isotropic shift $\delta$, shift anisotropy $\Delta\delta$ and asymmetry parameter $\eta$) (Fig. 4g-i). For each of the three nuclei, within each pair one

signal (I, III and VI) possesses a larger isotropic shift and shift anisotropy compared to the second (II, IV and V). We can tentatively assign the former set of three signals to the same $SiMe_3$ group, and the latter set of signals to the other $SiMe_3$ group. This interpretation is supported by a transferred-echo double resonance (TEDOR) experiment[78] (Fig. 5a), which displays a first unambiguous correlation between I and III, a second unambiguous correlation between II and IV, and no other correlations. These solid-state NMR spectra and our tentative interpretation indicate that each group of $^{1}H$, $^{13}C$ and $^{29}Si$ resonances represents a single $SiMe_3$ group in which there are rotations about the $C_1$-Si bond and about the Si-C bonds of each of the three methyls. The rate constants describing each rotation are larger than the spread of the individual chemical shifts of the exchanging sites.

If the tentative assignment is correct, this would indicate that the two resonances corresponding to $C_1$ and $H_1$ are absent from all the NMR spectra. This may be due to a severe reduction of sensitivity due to the large paramagnetic relaxation enhancement expected for these nuclei in close proximity to Yb, or due to the fact that potentially large shifts push them out of the excitation window. Moon and Patchkovski[41] and Vaara et al.[42–44] have developed a formalism to calculate the shift tensor in paramagnetic systems from the EPR tensors. We used this formalism with the $g$ tensor and hyperfine $A$ tensor assigned to $H_1$ that were extracted from both the CW and HYSCORE spectra to predict the expected shift for $H_1$. Since the HYSCORE spectra indicate that the $z$ axes of the principal axes frame (PAF) of the $g$ and $A$ tensor have a fixed relative orientation of 45°, the PAF of the A tensor needs to be transformed to the PAF of the $g$ tensor, and subsequently rotated again considering a distribution of Euler angles (ZYZ convention) with $\beta$ fixed at 45°. This still leaves two unknown Euler angles, which are systematically sampled over the full allowed range. Thereby, we predicted a range of possible shifts between 225 and 200 ppm, as shown in Fig. 5b. A shift in this range was not seen in any of the $^{1}H$ NMR spectra (1D, aMAT, TEDOR), therefore we conclude that we did not observe any NMR signal from $H_1$.

In order to confirm our tentative interpretation and provide a site-specific assignment,

we calculated the NMR shift tensors of all the spin-active nuclei in the complex. The total NMR shift can be expressed as:

$$\delta = \delta_{\mathrm{orb}} + \delta_{\mathrm{con}} + \delta_{\mathrm{pcs}} + \delta_{\mathrm{pcs,lr}} \ , \tag{1}$$

where $\delta_{\mathrm{orb}}$ corresponds to the orbital chemical shift, i.e. the contribution from the orbital motion of the electrons. $\delta_{\mathrm{con}}$ is the Fermi contact (FC) shift due to the through-bond hyperfine interaction, $\delta_{\mathrm{pcs}}$ and $\delta_{\mathrm{pcs,lr}}$ are the intra- and inter-molecular pseudo-contact shift (PCS) due to the through-space hyperfine interactions, respectively.

The orbital terms were calculated at the meta-GGA level of theory with the TPSS functional.[82] The terms $\delta_{\mathrm{con}} + \delta_{\mathrm{pcs}}$ were calculated following the formalism of Moon and Patchkovski[41] and Vaara et al.,[42–44] using the previously calculated $A$ and $g$ tensors. Long-range pseudo-contact shifts, $\delta_{\mathrm{pcs,lr}}$, were modeled considering a point-dipole approximation (see SI chapter 5 for more details).

Finally, in accordance with the tentative assignment of the experimental data, a 3-site fast exchange model was employed to average the shift tensors both within the methyl groups (along the Si-$C_i$ bonds) and the $Me_3Si$ groups (along the $C_1$-Si bond). The total computed shift tensors are summarized in Tab. 2.

Table 2: Calculated and experimental SA parameters for the proximal ($Me_3Si_{(2)}$) and distal ($Me_3Si_{(1)}$) $Me_3Si$ groups of $Yb[CH(SiMe_3)_2]_3$ in the Haeberlen convention[76] (experimental spectra are shown in Fig. 4). The calculated SAs were decomposed according to equation 1 using the formalism of Moon and Patchkovski[41] and Vaara et al.[42–44] Hyperfine tensors are calculated at post Hartree-Fock spin-component scaled MP2 level of theory, orbital chemical shifts with TPSS meta-GGA functional and $g$ tensor with multi-reference perturbation theory (CASSCF+NEVPT2). Similar trends are observed with NMR shifts computed with hyperfine tensors calculated at hybrid-GGA level of theory (see Tab. S13). $^{13}C$ and $^{1}H$ tensors of the $Me_3Si$ groups were averaged both within the methyl groups (along the Si-$C_i$ bonds) and the $Me_3Si$ groups (along the $C_1$-Si bond). Isotropic shifts were averaged considering the three different $SiMe_3$ groups, which due to small deviations of $C_{3v}$ symmetry in the optimized geometry result in differences in the SA tensors. These deviations account for the range of anisotropies $\Delta\delta$ and asymmetry $\eta$ parameters. Full list SA parameters is given in SI chapter 5.

| | Environment | $\delta_{\text{con}}$ | $\delta_{\text{pcs}}$ | $\delta_{\text{pcs,lr}}$ | $\delta_{\text{orb}}$ | $\delta$ | $\Delta\delta$ | $\eta$ |
|---|---|---|---|---|---|---|---|---|
| $^{1}H$ | $Me_3Si_{(2)}$ (Calc) | −1.0 | 6.9 | 1.0 | 2.2 | 9.0 | [79.4, 87.0] | [0.6, 0.7] |
| | (Site II) | | | | | $30 \pm 20$ | $153 \pm 1$ | $0.31 \pm 0.02$ |
| | $Me_3Si_{(1)}$ (Calc) | −0.1 | 2.2 | 0.9 | 2.0 | 5.0 | [39.5, 41.2] | [0.6, 0.7] |
| | (Site I) | | | | | $-20 \pm 20$ | $-56 \pm 1$ | $0.6 \pm 0.1$ |
| $^{13}C$ | $Me_3Si_{(2)}$ (Calc) | −0.2 | −4.6 | 0.9 | 5.1 | 1.2 | [−103.3, 105.8] | [0.7, 1.0] |
| | (Site IV) | | | | | $40 \pm 20$ | $-183 \pm 4$ | $0.4 \pm 0.1$ |
| | $Me_3Si_{(1)}$ (Calc) | −8.7 | 0.9 | 0.9 | 2.0 | −4.9 | [−51.3, 49.7] | [0.9, 1.0] |
| | (Site III) | | | | | $-20 \pm 20$ | $140[+30, -270]$ | $0.8 \pm 0.3$ |
| $^{29}Si$ | $Me_3Si_{(2)}$ (Calc) | −30.3 | −68.2 | 0.9 | −5.6 | −103.2 | [−237.2, −188.7] | 0.3 |
| | (Site V) | | | | | $-220 \pm 30$ | $-542 \pm 3$ | $0.74 \pm 0.01$ |
| | $Me_3Si_{(1)}$ (Calc) | −47.7 | −9.7 | −0.8 | −2.1 | −58.7 | [−218.7, 124.7] | [0.3, 0.9] |
| | (Site VI) | | | | | $-30 \pm 30$ | $409 \pm 3$ | $0.51 \pm 0.03$ |

We note that there are quantitative discrepancies between the experimental and computed shift tensor values, likely due to the shortcomings in calculation methods for the Fermi contact term, the complexity of the Yb electronic structure,[83] the neglect of the spin-orbit contributions to the hyperfine tensor, and the simplified nature of our dynamic hopping model. We note that consistent trends in the shift anisotropy parameters were observed when considering the hyperfine tensor calculated at hybrid DFT level of theory (see Tab. S14).

Despite these discrepancies, however, we do observe that the magnitude of the shifts and shift anisotropies for the nuclear species from the $Me_3Si_{(2)}$ group are consistently larger than those from the $Me_3Si_{(1)}$ group. For Si, this is a straightforward consequence of $Si_2$ being in closer proximity to Yb than $Si_1$. A pictorial representation of these computed tensors superimposed to the DFT-optimized structure is shown in Fig. 6. For $^{1}H$ and $^{13}C$, this

can be understood according to our dynamic model, where upon rotation about the $C_1$-Si bond, the three methyls on $Si_2$ are on average closer to the Yb ion than those on $Si_1$. This is therefore evidence that the same structural distortions, observed in the low-temperature XRD structure and associated with the presence of 3c-2e Yb–Me–Si interaction, persist at the higher temperature of the solid-state NMR measurements (ca. 300 K). Therefore, the $Yb[CH(SiMe_3)_2]_3$ complex possesses the $Yb\cdots C_\gamma$ interaction, described as a pseudo bridging Yb-Me-Si group and previously observed[21] for $Lu[CH(SiMe_3)_2]_3$ (see Fig. 1), at both low- and room-temperature and irrespective of the presence of the incomplete electronic $f$-shell.

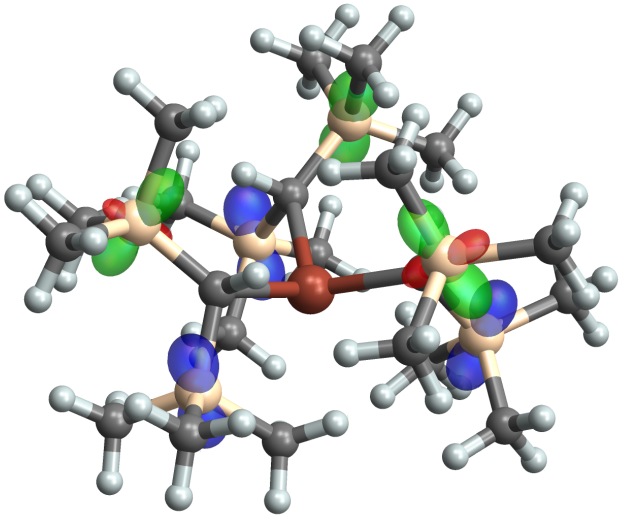

Figure 6: DFT-optimized structure of $Yb[CH(SiMe_3)_2]_3$ complex overlapped with ovaloid surface representations of the $^{29}$Si NMR tensors in shift convention (proximal $Me_3Si$ groups colored in green/red and distal $Me_3Si$ groups in blue/yellow).[84] The radius from the center of the tensor to a point on the ovaloid surface is proportional to the chemical shift when the magnetic field is aligned along that direction in space, and the sign of the shift is indicated by the color of the surface, red/yellow corresponds to positive shift and green/blue to a negative shift.

## Conclusions

In summary, low-temperature XRD, magnetic susceptibility measurements, pulsed EPR, solid-state NMR and quantum-chemical calculations solved both the molecular and electronic structure of the paramagnetic ytterbium alkyl compound $Yb[CH(SiMe_3)_2]_3$. These

four techniques were shown to be complementary, each one revealing specific aspects of the geometry or the electronic structure at different temperatures.

The XRD data for $Yb[CH(SiMe_3)_2]_3$ contains short distances between Yb and one carbon in one of the silyl groups ($Yb\cdots C_\gamma$), consistent with a three-center - two-electron Yb–Me–Si interaction that was also observed in the diamagnetic Lu analogue. This experimental structure was supplemented by relativistic DFT calculations, which added the position of the protons and constrained bonds and angles around the proximal silyl group. In particular, this computed structure allowed us to determine the positions of the $\alpha$-H atoms of the three $CH(SiMe_3)_2$ ligands, which were otherwise accessible only indirectly by experiments. These $\alpha$-H atoms participate in acute Yb-C-H angles, associated to the electrostatic repulsion from the surrounding electropositive Yb and Si atoms.

The characterization of the electronic structure was made possible by low-temperature EPR and room-temperature paramagnetic NMR spectroscopies. EPR revealed a significant hyperfine coupling between the Yb ion and the $\alpha$-H spins in its first coordination sphere, allowing also to confirm the positions of the $\alpha$-H atoms, determined from the relativistic DFT optimization. In combination with multi-reference perturbation theory calculations and magnetic susceptibility measurements, the EPR data indicated that the electronic structure of the complex is close to that of the Yb(III) free ion with a single configuration of $4f^{13}$ ($^2F_{7/2}$).

Paramagnetic MAS NMR revealed two sets of signals for all $^1H$, $^{13}C$ and $^{29}Si$ spins further away from the Yb ion. This is consistent with a dynamical behavior of the ligand at room temperature, but also with a persistent distortion of the coordination of the proximal $SiMe_3$ group with significantly less symmetry. This confirms that the secondary metal-ligand interaction, referred to as the three-center - two-electron Yb–Me–Si interaction is present in the structure of $Yb[CH(SiMe_3)_2]_3$ at both low and room temperatures. These structural features are favored by the electropositive nature of the Yb(III) ion, being likely a general feature of lanthanide metal-alkyl complexes. At the same time, the partially filled $f$-shell of

the Yb atom in $Yb[CH(SiMe_3)_2]_3$ does not significantly influence its bonding properties.

This study integrates state-of-the-art achievements in magnetic resonance spectroscopies, inorganic and computational chemistry. Besides reporting the preparation on a large scale of the paramagnetic ytterbium alkyl compound $Yb[CH(SiMe_3)_2]_3$, this study represents the first study of the structure and electronic properties of an Yb complex in the solid-state by convergent use of XRD, EPR, solid-state NMR and quantum chemistry, which allows correlation of low-temperature geometry with room-temperature behavior. It contains the prediction of NMR shift tensors of a lanthanide complex in the solid state with sufficient accuracy to permit the assignment of the experimental resonances and their constructive interpretation. It presents the experimental signature of a secondary metal-ligand interaction in a lanthanide paramagnetic species. Overall, this work demonstrates the crucial importance of employing complementary atomic-resolution techniques to solve structural problems in chemistry. More specifically, it pushes the frontier for characterization of organometallic complexes towards paramagnetic lanthanide complexes, which so far have been intractable at this level of precision.

## Acknowledgement

We acknowledge Laurent Maron (Université Paul Sabatier, Toulouse) for discussions at the early stage of this project. We acknowledge Maciej Korzynski (ETHZ) for a help with preparation of the manuscript. We acknowledge Elizaveta A. Suturina (University of Bath) and Aleksander Jaworski (Stockholm University) for the advices concerning quantum chemistry calculations in lanthanide complexes. We thank Martin Bröring (Institut für Anorganische und Analytische Chemie) at TU Braunschweig for providing access to the SQUID magnetometer.

## Supporting Information Available

## Supporting Information

The Supporting Information is available.

## Author Information

Richard A. Andersen unfortunately passed away on June 16, 2019 while the early draft of this manuscript was being written; this manuscript is dedicated to his memory.

## Corresponding Authors

∗ andrew.pell@ens-lyon.fr; ccoperet@ethz.ch; gjeschke@ethz.ch; guido.pintacuda@ens-lyon.fr

## Author contribution

A.A. and D.K. performed EPR measurements. F.A. and M.P.C. developed the synthetic procedures. J.P.C. and K.J.S. conducted NMR measurements. J.P.C. and A.A. performed quantum chemical calculations. M.W. and F.A. performed XRD studies. D.B. and M.D.W. conducted magnetic susceptibility measurements. M.D.W., A.J.P., C.C., G.J., G.P. and R.A.A. supervised the project. All authors participated in writing the manuscript. A.A., F.A., J.P.C., K.J.S. and M.P.C. declare equal contribution.

## Funding Sources

A.A. is supported by a SNF - ANR grant (Mr. CAT 2-77275-15). J. P. C. is supported by the Swedish Research Council (2016-03441) and by the Agence Nationale de la Recherche (ANR-

21-CE29-0010-01. The computations were enabled by resources provided by the Swedish National Infrastructure for Computing (SNIC) at HPC2N, project number 2021-5-122.

# References

(1) Hartwig, J. *Organotransition Metal Chemistry: From Bonding to Catalysis*; University Science Books, Mill Valley, California, 2010.

(2) Wilkinson, G.; Stone, G. A.; Abel, E. W. *Comprehensive organometallic chemistry: The synthesis, reactions, and structures of organometallic compounds*; Pergamon Press, 1982.

(3) Lukens, W. W.; Smith, M. R.; Andersen, R. A. A $\pi$-Donor Spectrochemical Series for X in $(Me_5C_5)_2TiX$, and $\beta$-Agostic Interactions in X = Et and N(Me)Ph. *J. Am. Chem. Soc.* **1996**, *118*, 1719–1728.

(4) Gordon, C. P.; Shirase, S.; Yamamoto, K.; Andersen, R. A.; Eisenstein, O.; Copéret, C. NMR chemical shift analysis decodes olefin oligo- and polymerization activity of $d^0$ group 4 metal complexes. *Proc. Natl. Acad. Sci. USA* **2018**, *115*, 5867–5876.

(5) Clauss, K.; Beermann, C. Halogenfreie Methyl-Verbindungen des Titans und Chroms. *Angew. Chem. Int. Ed. Engl.* **1959**, *71*, 627–627.

(6) Berthold, H. J.; Groh, G. Preparation of Tetramethylzirconium, $Zr(CH_3)_4$. *Angew. Chem. Int. Ed. Engl.* **1966**, *5*, 516–516.

(7) Morrow, M. K. *Synthesis and characterization of tetramethylhafnium*; Thesis submitted to University of Tennessee, Knoxville, 1970.

(8) Schrock, R. R. Preparation and characterization of $M(CH_3)_5$ (M = Nb or Ta) and $Ta(CH_2C_6H_5)_5$ and evidence for decomposition by $\alpha$-hydrogen atom abstraction. *J. Organomet. Chem.* **1976**, *112*, 209–225.

(9) Roessler, B.; Kleinhenz, S.; Seppelt, K. Pentamethylmolybdenum. *Chem. Commun.* **2000**, 1039–1040.

(10) Shortland, A. J.; Wilkinson, G. Preparation and properties of hexamethyltungsten. *Dalton Trans.* **1973**, 872–876.

(11) Phennig, V.; Seppelt, K. Crystal and Molecular Structures of Hexamethyltungsten and Hexamethylrhenium. *Science* **1996**, *271*, 626–628.

(12) Demolliens, A.; Jean, Y.; Eisenstein, O. Deviation from the ideal octahedral field vs. alkyl distortion in d0 metal-alkyl complexes: a MO study. *Organometallics* **1986**, *5*, 872–876.

(13) Mowat, W.; Shortland, A. J.; Hill, N. J.; Wilkinson, G. Elimination stabilized alkyls. Part II. Neopentyl and related alkyls of chromium(IV). *Dalton Trans.* **1973**, 770–778.

(14) Mowat, W.; Shortland, A. J.; Hill, N. J.; Wilkinson, G. Elimination stabilized alkyls. Part III. Trimethylsilylmethyl and neopentyl alkyls of transition metals. *Dalton Trans.* **1973**, 1120–1124.

(15) Schrock, R. R.; Fellmann, J. D. Multiple Metal-Carbon Bonds. 8. Preparation, Characterization, and Mechanism of Formation of the Tantalum and Niobium Neopentylidene Complexes, M(CH2CMe3)3(CHCMe3). *J. Am. Chem. Soc.* **1978**, *100*, 3359–3370.

(16) Schrock, R. R. High-Oxidation-State Molybdenum and Tungsten Alkylidyne Complexes. *Acc. Chem. Res.* **1986**, *19*, 342–348.

(17) Edwards, D. S.; Biondi, L. V.; Zillen, J. W.; Churchill, M. R.; R., S. R. Rhenium(VII) neopentylidene and neopentylidyne complexes and the x-ray structure of Re(CCMe3)(CHCMe3)(C5H5N)2. *Organometallics* **1983**, *2*, 1505–1513.

(18) Brookhart, M.; Green, M. L. H.; Wong, L.-L. Carbon-Hydrogen-Transition Metal Bonds. *Prog. Inorg. Chem.* **1988**, *36*, 1–124.

(19) Avent, A. G.; Caro, C. F.; Hitchcock, P. B.; Lappert, M. F.; Li, Z.; Wei, X.-H. Synthetic and structural experiments on yttrium, cerium and magnesium trimethylsilylmethyls and their reaction products with nitriles; with a note on two cerium $\beta$-diketiminates. *Dalton Trans.* **2004**, 1567–1577.

(20) Hitchcock, P. B.; Lappert, M. F.; Smith, R. G.; Bartlett, R. A.; Power, P. P. Synthesis and structural characterisation of the first neutral homoleptic lanthanide metal (III) alkyls:[$LnR_3$][Ln= La or Sm, R= CH ($SiMe_3$)$_2$]. *J. Chem. Soc., Chem. Commun.* **1988**, 1007–1009.

(21) Conley, M. P.; Lapadula, G.; Sanders, K.; Gajan, D.; Lesage, A.; Del Rosal, I.; Maron, L.; Lukens, W. W.; Coperet, C.; Andersen, R. A. The nature of secondary interactions at electrophilic metal sites of molecular and silica-supported organolutetium complexes from solid-state NMR spectroscopy. *J. Am. Chem. Soc.* **2016**, *138*, 3831–3843.

(22) Eaborn, C.; Hitchcock, P. B.; Izod, K.; Smith, J. D. A Monomeric Solvent-Free Bent Lanthanide Dialkyl and a Lanthanide Analog of a Grignard Reagent. Crystal Structures of Yb{$C(SiMe_3)_3$}$_2$ and [Yb{$C(SiMe_3)_3$}I·$OEt_2$]$_2$. *J. Am. Chem. Soc.* **1994**, *26*, 12071–12072.

(23) Evans, W. J.; Anwander, R.; Ziller, J. W. Inclusion of $Al_2Me_6$ in the Crystalline Lattice of the Organometallic Complexes $LnAl_3Me_{12}$. *Organometallics* **1995**, *14*, 1107–1109.

(24) Yan, K.; Upton, B. M.; Ellern, A.; Sadow, A. D. Lewis Acid-Mediated $\beta$-Hydride Abstraction Reactions of Divalent M($C(SiHMe_2)_3$)$_2$$THF_2$ (M = Ca, Yb). *J. Am. Chem. Soc.* **2009**, *131*, 15110–15111.

(25) Yan, K.; Pawlikowski, A. V.; Ebert, C.; Sadow, A. D. A tris(alkyl)yttrium compound containing six $\beta$-agostic Si–H interactions. *Chem. Commun.* **2009**, 656–658.

(26) Brookhart, M.; Green, M. L. H.; Parkin, G. Agostic interactions in transition metal compounds. *Proc. Natl. Acad. Sci. USA* **2007**, *104*, 6908–6914.

(27) Longuet-Higgins, H. C. The structure of some electron-deficient molecules. *J. Chem. Soc.* **1946**, 139–143.

(28) Brookhart, M.; Green, M. L. H.; Parkin, G. Molecular structure and bonding in hexamethyldialuminum. *Proc. Natl. Acad. Sci. USA* **2007**, *104*, 6908–6914.

(29) Klooster, W. T.; Lu, R. S.; Anwander, R.; Evans, W. J.; Koetzle, T. F.; Bau, R. Neutron Diffraction Study of $[Nd(AlMe_4)_3]\cdot 0.5\cdot Al_2Me_6$ at 100 K: The First Detailed Look at a Bridging Methyl Group with a Trigonal-Bipyramidal Carbon Atom. *Angew. Chem. Int. Ed. Engl.* **1998**, *37*, 1268–1270.

(30) Halbach, R. L.; Nocton, G.; Booth, C. H.; Maron, L.; Andersen, R. A. Cerium Tetrakis(tropolonate) and Cerium Tetrakis(acetylacetonate) Are Not Diamagnetic but Temperature-Independent Paramagnets. *Inorg. Chem.* **2018**, *57*, 7290–7298.

(31) Halbach, R. L.; Nocton, G.; Amaro-Estrada, J. I.; Maron, L.; Booth, C. H.; Andersen, R. A. Understanding the Multiconfigurational Ground and Excited States in Lanthanide Tetrakis Bipyridine Complexes from Experimental and CASSCF Computational Studies. *Inorg. Chem.* **2019**, *58*, 12083–12098.

(32) Booth, C. H.; Walter, M. D.; Kazhdan, D.; Hu, Y.-J.; Lukens, W. W.; Bauer, E. D.; Maron, L.; Eisenstein, O.; Andersen, R. A. Decamethylytterbocene complexes of bipyridines and diazabutadienes: Multiconfigurational ground states and open-shell singlet formation. *J. Am. Chem. Soc.* **2009**, *131*, 6480–6491.

(33) Booth, C. H.; Kazhdan, D.; Werkema, E. L.; Walter, M. D.; Lukens, W. W.; Bauer, E. D.; Hu, Y.-J.; Maron, L.; Eisenstein, O.; Head-Gordon, M. Intermediate-valence tautomerism in decamethylytterbocene complexes of methyl-substituted bipyridines. *J. Am. Chem. Soc.* **2010**, *132*, 17537–17549.

(34) Denning, R. G.; Harmer, J.; Green, J. C.; Irwin, M. Covalency in the 4f Shell of tris-Cyclopentadienyl Ytterbium ($YbCp_3$) - A Spectroscopic Evaluation. *J. Am. Chem. Soc.* **2011**, *133*, 20644–20660.

(35) Walter, M. D.; Matsunaga, P. T.; Burns, C. J.; Maron, L.; Andersen, R. A. Synthesis and Reactions of $[Cp^\star_2Yb]_2$($\mu$-Me and $[Cp^\star_2Yb]_2$($\mu$-Me(Me) and Related $Yb_2$(II, III) and $Yb_2$ (III, III) Compounds. *Organometallics* **2017**, *36*, 4564–4578.

(36) Gordon, C. P.; Culver, D. B.; Conley, M. P.; Eisenstein, O.; Andersen, R. A.; Copéret, C. $\pi$-Bond Character in Metal-Alkyl Compounds for C-H Activation: How, When, and Why? *J. Am. Chem. Soc.* **2011**, *141*, 648–656.

(37) Roos, B. O.; Pyykkö, P. Bonding Trends in Molecular Compounds of Lanthanides: The Double-Bonded Carbene Cations $LnCH_2^+$ (Ln= Sc, Y, La–Lu). *Chem. Eur. J.* **2010**, *16*, 270–275.

(38) Tian, S.; Arredondo, V. M.; Stern, C. L.; Marks, T. J. Constrained geometry organolanthanide catalysts. Synthesis, structural characterization, and enhanced aminoalkene hydroamination/cyclization activity. *Organometallics* **1999**, *18*, 2568–2570.

(39) Pell, A. J.; Pintacuda, G.; Grey, C. P. Paramagnetic NMR in solution and the solid state. *Prog. Nucl. Magn. Reson. Spectrosc.* **2019**, *111*, 1–271.

(40) Roessler, M. M.; Salvadori, E. Principles and applications of EPR spectroscopy in the chemical sciences. *Chem. Soc. Rev.* **2018**, *47*, 2534–2553.

(41) Moon, S.; Patchkovskii, S. *Calculation of NMR and EPR Parameters*; John Wiley & Sons, Ltd, 2004; Chapter 20, pp 325–338.

(42) Pennanen, T. O.; Vaara, J. Density-functional calculations of relativistic spin-orbit effects on nuclear magnetic shielding in paramagnetic molecules. *J. Chem. Phys.* **2005**, *123*, 174102.

(43) Pennanen, T. O.; Vaara, J. Nuclear magnetic resonance chemical shift in an arbitrary electronic spin state. *Phys. Rev. Lett.* **2008**, *100*, 133002.

(44) Vaara, J.; Rouf, S. A.; Mares, J. Magnetic couplings in the chemical shift of paramagnetic NMR. *J. Chem. Theory Comput.* **2015**, *11*, 4840–4849.

(45) Parigi, G.; Benda, L.; Ravera, E.; Romanelli, M.; Luchinat, C. Pseudocontact shifts and paramagnetic susceptibility in semiempirical and quantum chemistry theories. *J. Chem. Phys.* **2019**, *150*, 144101.

(46) Lang, L.; Ravera, E.; Parigi, G.; Luchinat, C.; Neese, F. Solution of a puzzle: High-level quantum-chemical treatment of pseudocontact chemical shifts confirms classic semiempirical theory. *J. Phys. Chem. Lett.* **2020**, *11*, 8735–8744.

(47) Rouf, S. A.; Mares, J.; Vaara, J. $^{1}$H chemical shifts in paramagnetic Co(II) pyrazolylborate complexes: A first-principles study. *J. Chem. Theory Comput.* **2015**, *11*, 1683–1691.

(48) Pigliapochi, R.; Pell, A. J.; Seymour, I. D.; Grey, C. P.; Ceresoli, D.; Kaupp, M. DFT investigation of the effect of spin-orbit coupling on the NMR shifts in paramagnetic solids. *Phys. Rev. B* **2017**, *95*, 054412.

(49) Mondal, A.; Gaultois, M. W.; Pell, A. J.; Iannuzzi, M.; Grey, C. P.; Hutter, J.; Kaupp, M. Large-scale computation of nuclear magnetic resonance shifts for paramagnetic solids using CP2K. *J. Chem. Theory Comput.* **2018**, *14*, 377–394.

(50) Mondal, A.; Kaupp, M. Computation of NMR shifts for paramagnetic solids including zero-field-splitting and beyond-DFT approaches. Application to $LiMPO_4$ (M= Mn, Fe, Co, Ni) and $MPO_4$ (M= Fe, Co). *J. Phys. Chem. C* **2019**, *123*, 8387–8405.

(51) Pyykkönen, A.; Feher, R.; Köhler, F. H.; Vaara, J. Paramagnetic Pyrazolylborate Com-

plexes Tp2M and Tp* 2M: $^{1}$H, $^{13}$C, $^{11}$B, and $^{14}$N NMR Spectra and First-Principles Studies of Chemical Shifts. *Inorg. Chem.* **2020**, *59*, 9294–9307.

(52) Andersen, A. B.; Pyykkönen, A.; Jensen, H. J. A.; McKee, V.; Vaara, J.; Nielsen, U. G. Remarkable reversal of $^{13}$C-NMR assignment in $d^1$, $d^2$ compared to $d^8$, d9 acetylacetonate complexes: analysis and explanation based on solid-state MAS NMR and computations. *Phys. Chem. Chem. Phys.* **2020**, *22*, 8048–8059.

(53) Ashuiev, A.; Allouche, F.; Wili, N.; Searles, K.; Klose, D.; Copéret, C.; Jeschke, G. Molecular and supported Ti(III)-alkyls: efficient ethylene polymerization driven by the $\pi$-character of metal-carbon bonds and back donation from a singly occupied molecular orbital. *Chem. Sci.* **2021**, *12*, 780–792.

(54) Tecle, B.; Maqsudur Rahman, A. F. M.; Oliver, J. P. X-ray crystal structure of trimethylsilylmethyllithium. *J. Organomet. Chem.* **1986**, *317*, 267–275.

(55) Höfer, P.; Grupp, A.; Nebenführ, H.; Mehring, M. Hyperfine sublevel correlation (hyscore) spectroscopy: a 2D ESR investigation of the squaric acid radical. *Chem. Phys. Lett.* **1986**, *132*, 279–282.

(56) Schosseler, P.; Wacker, T.; Schweiger, A. Pulsed ELDOR Detected NMR. *Chem. Phys. Lett.* **1994**, *224*, 319–324.

(57) Allouche, F.; Klose, D.; Gordon, C. P.; Ashuiev, A.; Wörle, M.; Kalendra, V.; Mougel, V.; Copéret, C.; Jeschke, G. Low-Coordinated Titanium (III) Alkyl—Molecular and Surface—Complexes: Detailed Structure from Advanced EPR Spectroscopy. *Angew. Chem. Int. Ed. Engl.* **2018**, *130*, 14741–14745.

(58) Perdew, J. P.; Ernzerhof, M.; Burke, K. Rationale for mixing exact exchange with density functional approximations. *J. Chem. Phys.* **1996**, *105*, 9982–9985.

(59) Becke, A. Density-functional thermochemistry. III. The role of exact exchange. *J. Chem. Phys* **1993**, *98*, 5648.

(60) Adamo, C.; Barone, V. Toward reliable density functional methods without adjustable parameters: The PBE0 model. *J. Chem. Phys.* **1999**, *110*, 6158–6170.

(61) Grimme, S.; Antony, J.; Ehrlich, S.; Krieg, H. A consistent and accurate ab initio parametrization of density functional dispersion correction (DFT-D) for the 94 elements H-Pu. *J. Chem. Phys* **2010**, *132*, 154104.

(62) Lenthe, E. v.; Baerends, E.-J.; Snijders, J. G. Relativistic regular two-component Hamiltonians. *J. Chem. Phys* **1993**, *99*, 4597–4610.

(63) Siegbahn, P.; Heiberg, A.; Roos, B.; Levy, B. A comparison of the super-CI and the Newton-Raphson scheme in the complete active space SCF method. *Phys. Scr.* **1980**, *21*, 323.

(64) Roos, B. O.; Taylor, P. R.; Sigbahn, P. E. A complete active space SCF method (CASSCF) using a density matrix formulated super-CI approach. *Chem. Phys.* **1980**, *48*, 157–173.

(65) Siegbahn, P. E.; Almlöf, J.; Heiberg, A.; Roos, B. O. The complete active space SCF (CASSCF) method in a Newton–Raphson formulation with application to the HNO molecule. *J. Chem. Phys.* **1981**, *74*, 2384–2396.

(66) Angeli, C.; Cimiraglia, R.; Evangelisti, S.; Leininger, T.; Malrieu, J.-P. Introduction of n-electron valence states for multireference perturbation theory. *J. Chem. Phys.* **2001**, *114*, 10252–10264.

(67) Angeli, C.; Cimiraglia, R.; Malrieu, J.-P. n-electron valence state perturbation theory: A spinless formulation and an efficient implementation of the strongly contracted and of the partially contracted variants. *J. Chem. Phys.* **2002**, *117*, 9138–9153.

(68) Angeli, C.; Pastore, M.; Cimiraglia, R. New perspectives in multireference perturbation theory: the n-electron valence state approach. *Theor. Chem. Account* **2007**, *117*, 743–754.

(69) Reiher, M. Douglas-Kroll-Hess Theory: a relativistic electrons-only theory for chemistry. *Theor. Chem. Acc.* **2006**, *116*, 241–252.

(70) Fink, R. F. Spin-component-scaled Møller–Plesset (SCS-MP) perturbation theory: a generalization of the MP approach with improved properties. *J. Chem. Phys* **2010**, *133*, 174113.

(71) Kossmann, S.; Neese, F. Correlated ab initio spin densities for larger molecules: orbital-optimized spin-component-scaled MP2 method. *J. Phys. Chem. A* **2010**, *114*, 11768–11781.

(72) Carvalho, J. P.; Jaworski, A.; Brady, M. J.; Pell, A. J. Separation of quadrupolar and paramagnetic shift interactions with TOP-STMAS/MQMAS in solid-state lighting phosphors. *Magn. Reson. Chem.* **2020**, *58*, 1055–1070.

(73) Ma, Z.; Lu, C.; Chen, J.; Rokicińska, A.; Kuśtrowski, P.; Coridan, R.; Dronskowski, R.; Slabon, A.; Jaworski, A. $CeTiO_2N$ oxynitride perovskite: paramagnetic $^{14}N$ MAS NMR without paramagnetic shifts. *Zeitschrift für Naturforschung B* **2021**, *76*, 275–280.

(74) Jaworski, A.; Hedin, N. Electron correlation and vibrational effects in predictions of paramagnetic NMR shifts. *Phys. Chem. Chem. Phys.* **2022**, *24*, 15230–15244.

(75) Feng, R.; Duignan, T. J.; Autschbach, J. Electron-Nucleus Hyperfine Coupling Calculated from Restricted Active Space Wavefunctions and an Exact Two-Component Hamiltonian. *J. Chem. Theory Comput.* **2021**, *17*, 255–268.

(76) Haeberlen, U. *Advances in magnetic resonance*; Academic Press, 1976; Vol. 1.

(77) Clément, R. J.; Pell, A. J.; Middlemiss, D. S.; Strobridge, F. C.; Miller, J. K.; Whittingham, M. S.; Emsley, L.; Grey, C. P.; Pintacuda, G. Spin-transfer pathways in paramagnetic lithium transition-metal phosphates from combined broadband isotropic solid-state MAS NMR spectroscopy and DFT calculations. *J. Am. Chem. Soc.* **2012**, *134*, 17178–17185.

(78) Kervern, G.; Pintacuda, G.; Zhang, Y.; Oldfield, E.; Roukoss, C.; Kuntz, E.; Herdtweck, E.; Basset, J.-M.; Cadars, S.; Lesage, A. Solid-state NMR of a paramagnetic DIAD-FeII catalyst: Sensitivity, resolution enhancement, and structure-based assignments. *J. Am. Chem. Soc.* **2006**, *128*, 13545–13552.

(79) Zaremba, S. K. Good lattice points, discrepancy, and numerical integration. *Annali di Matematica* **1966**, *73*, 293–317.

(80) Conroy, H. Molecular Schrödinger equation. VIII. A new method for the evaluation of multidimensional integrals. *J. Chem. Phys.* **1967**, *47*, 5307–5318.

(81) Cheng, V. B.; Suzukawa Jr, H. H.; Wolfsberg, M. Investigations of a nonrandom numerical method for multidimensional integration. *J. Chem. Phys.* **1973**, *59*, 3992–3999.

(82) Tao, J.; Perdew, J. P.; Staroverov, V. N.; Scuseria, G. E. Climbing the density functional ladder: Nonempirical meta-generalized gradient approximation designed for molecules and solids. *Phys. Rev. Lett.* **2003**, *91*, 146401.

(83) Autschbach, J.; Patchkovskii, S.; Pritchard, B. Calculation of hyperfine tensors and paramagnetic NMR shifts using the relativistic zeroth-order regular approximation and density functional theory. *J. Chem. Theory Comput.* **2011**, *7*, 2175–2188.

(84) Young, R. P.; Lewis, C. R.; Yang, C.; Wang, L.; Harper, J. K.; Mueller, L. J. TensorView: A software tool for displaying NMR tensors. *Magn. Reson. Chem.* **2019**, *57*, 211–223.